Three-dimensionality of one- and two-layer electromagnetically driven thin-layer flows

Jeffrey Tithof, Benjamin C. Martell, and Douglas H. Kelley*
Department of Mechanical Engineering, University of Rochester, Rochester, New York 14627, USA

(Received 18 January 2018; published 12 June 2018)

We measure and compare the out-of-plane motion in three experimental configurations for approximating two-dimensional flow with electromagnetically driven thin fluid layers. A prior study found that out-of-plane motion grows suddenly when the Reynolds number Re exceeds a critical value Re_c in a two-layer miscible configuration [Kelley and Ouellette, Phys. Fluids **23**, 045103 (2011)]. Here, we confirm that observation; however, we find that a similar onset does not occur in either a single-layer or two-layer immiscible configuration for the ranges $\mathrm{Re} < 520$ and $\mathrm{Re} < 740$, respectively. Below the critical Reynolds number, the three configurations have out-of-plane motion with similar magnitude. We confirm that two different normalized measures of out-of-plane motion show similar trends among the three configurations as Re varies. Finally, we compute the vertical velocity profiles using an analytical model of each of the three configurations and provide further evidence suggesting the transition observed in the miscible configuration is due to a shear instability. Our results lead to suggestions for future experimentalists: The single-layer and immiscible configurations most closely approximate two-dimensional flow over a wide range of Re, though the miscible configuration minimizes clumping of tracer particles.

DOI: 10.1103/PhysRevFluids.3.064602

I. INTRODUCTION

Two-dimensional (2D) fluid dynamics might at first seem an arcane topic for a world with three physical dimensions. But applications, theoretical predictions, and practicalities all give good reason to consider 2D flow. First, the topic is applicable because many real, three-dimensional (3D) flows are commonly approximated as 2D. Oceans and atmospheres, for example, have large aspect ratios that make two-dimensionality a reasonable first-order approximation. Additionally, geostrophic effects cause many behaviors characteristic of 2D flows to arise in geophysical flows [1]. In fact, the well-known Taylor-Proudman theorem asserts that steady flows dominated by rotation must be 2D [2]. Considering time-dependent flows with strong rotation, it can be shown that the linear eigenmodes of the equations of motion are Coriolis-restored inertial waves [3,4] whose spatial structures remain nearly 2D when the time dependence is weak [5]. Magnetic fields applied to flowing fluid that is electrically conductive also tend to make the motion 2D, as in the case of convection rolls aligning with magnetic fields [6,7].

Second, 2D fluid dynamics is an interesting topic because rich theories of turbulence in two dimensions make striking predictions that differ starkly from turbulence in three dimensions. Most notable is that the conservation of energy in 3D flows yields an inertial cascade of energy, transferred to smaller and smaller length scales. However, in two dimensions, both energy and enstrophy (squared vorticity) are conserved, so two cascades occur, including the inverse cascade of energy to *larger* length scales [8–10]. Third, 2D flows are far less expensive to simulate and allow for far

*d.h.kelley@rochester.edu

less cumbersome experimental diagnostics. Thus 2D flows are an especially appealing framework for exploring new dynamical systems approaches to characterizing turbulence, such as Lagrangian coherent structures (LCS) [11–13] and exact coherent structures (ECS) [14–16]. Insight gained in more tractable 2D flows may in turn shed light on the more onerous 3D ones.

For experimental studies of quasi-two-dimensional (Q2D) fluid dynamics, two approaches are most common. Soap films, whose motion is usually driven by gravity and whose boundaries are usually set by suspended strings or bars, approximate two-dimensionality well in that their aspect ratio is very large, on the order of 10^3 or more [17]. Because of their significant mean flow, soap films also lend themselves naturally to investigations informed by prior work in wind tunnels and water channels. The primary mechanism that causes soap films to deviate from 2D behavior, however, is significant spatial variation of thickness, which affects flow as well as the motion of tracer particles used to detect flow. In this paper, we will not consider soap films further; instead we commend readers to prior publications considering soap films as models for 2D flows [17–21].

Alternately, Q2D fluid flow can be driven electromagnetically in a thin layer of conductive fluid, usually by passing electrical current through the layer, with permanent magnets nearby [22,23]. Such thin-layer flows are less susceptible to complications from thickness variation, and the variety of achievable flow shapes is limited only by the arrangement of the magnets and current. However, because thin-layer flows are thicker than soap films (a few millimeters, compared to a few microns [24]), their aspect ratio is not as large and thus the boundaries do not constrain out-of-plane motion as strongly. If thin-layer flows are to give insight into 2D fluid dynamics, care must be taken to prevent and quantify out-of-plane motion.

To prevent out-of-plane motion, the first common technique is to make the fluid layer as thin as possible. Typically, the fluid layer may be as thin as 3 mm, but layers that are much thinner are difficult to work with, as surface tension tends to cause them to rupture. Because of their ease of implementation, thin single-layer configurations were devised first [22] and have since been used extensively [23,25,26]. Typically tracer particles, added to make flow visible and measurable, float on the surface. A second common technique thought to suppress out-of-plane motion is stratification. The miscible two-layer configuration [27–30] utilizes stratification in that it consists of a thin freshwater layer floating atop a thin electrolyte layer. The bottom layer is the test fluid and is electromagnetically driven, while the top layer, although not driven, is set in motion due to viscous coupling. Typically tracer particles float at the interface between fresh water and test fluid. Using miscible layers prevents surface tension at the interface from causing particles to clump. A further stratification-based improvement was made to the two-layer configuration by choosing immiscible fluids [31–33], with the justification that immiscibility should further suppress out-of-plane motion. Typically, this configuration consists of a conducting electrolyte layer above a denser lubricating dielectric fluid; here, the top layer is driven, but again both layers are set in motion due to viscous coupling.

A number of methods have been used to quantify out-of-plane motion, and the faithfulness of thin-layer flows as models for 2D fluid dynamics has been considered in a number of contexts, as reviewed by Clercx and Van Heijst [34]. One measure of two-dimensionality comes from comparing the flow decay time at the free surface to the flow decay time at an internal location. Paret *et al.* [35] used such decay time measurements in a checkerboard of vortices to conclude that after an initial transient, the vertical velocity profile was consistent with Poiseuille flow, suggesting good two-dimensionality. Jüttner *et al.* [36] performed numerical simulations using Poiseuille flow as an initial condition and found solutions that agreed well with experiments, again suggesting good two-dimensionality.

On the other hand, in 3D simulations of decaying monopolar vortices, Satijn *et al.* [37] found significant out-of-plane motion in thick layers and at high Reynolds numbers. A series of studies by Akkermans *et al.* [38–40] used both 3D simulations and stereoscopic particle image velocimetry to study monopolar vortices, finding a vertical profile inconsistent with Poiseuille flow and suggesting that such flows do not approximate two-dimensionality faithfully. Those authors often quantified out-of-plane motion using the measured divergence of the two-dimensional velocity field. In contrast,

Kelley and Ouellette [30] quantified out-of-plane motion using a method adapted from oceanography [41], in which 2D velocity measurements are projected onto stream function, boundary, and potential modes, and divergence need not be calculated directly. Studying a two-layer miscible configuration driven by a checkerboard of vortices, they found a critical Reynolds number Re_c above which out-of-plane motion increased rapidly, probably because of a shear instability. For Reynolds number $\mathrm{Re} < \mathrm{Re}_c$, they found weak out-of-plane motion increasing linearly with Re, probably driven by Ekman pumping.

In practical terms, those of us who design and operate thin-layer electromagnetically driven flows would like to know which configurations approximate 2D fluid dynamics most faithfully and the extent to which they deviate. Though these prior studies have provided useful data points for addressing those questions, the data points are isolated: Out-of-plane motion has been measured differently in different studies, and no studies have directly compared the out-of-plane motion among different fluid configurations. Here, we set out to rectify that situation. We have measured out-of-plane motion using both the projection-based method of Kelley and Ouellette [30] and the divergence-based method of Akkermans *et al.* [38,40], over a wide range of Re, using single-layer, two-layer miscible, and two-layer immiscible configurations. In all cases, we drove flow using the same checkerboard of vortices. For the miscible configuration, we found evidence of a critical Reynolds number above which out-of-plane motion grows rapidly stronger. For the single-layer and immiscible configurations, we found no such critical Reynolds number and similar magnitudes of out-of-plane motion. These results challenge the notion that stratification enhances two-dimensionality.

We also found that the two layers of the miscible configuration quickly mix at high Re, effectively resulting in a thicker single-layer configuration. Thus if two-dimensionality is the experimental goal, our results recommend the single-layer or immiscible configurations, which remain most nearly two-dimensional at high Reynolds numbers; the single-layer configuration may be preferable as it is simpler to prepare. However, if high spatial resolution (high particle density) is essential, the miscible configuration may be justified to prevent tracer particles from clumping, especially for low Re. We also provide evidence that the larger out-of-plane motion observed in the miscible configuration may be due to larger shear along the vertical direction, compared to the single-layer or immiscible configurations.

Below, the paper continues with a description of our experimental methods in Sec. II. We present the resulting measurements in Sec. III, showing instantaneous measurements from all three configurations as well as statistics of out-of-plane motion. Finally, we offer conclusions in Sec. IV, make suggestions regarding use of the three different configurations, and discuss future work.

II. EXPERIMENTAL METHODS

Our experimental apparatus, sketched in Fig. 1, is similar to devices described previously [30]. A thin layer of test fluid is contained laterally in a square vessel of size 254 × 254 mm. A lubrication layer or miscible layer may also be present, depending on which configuration is the subject of the experiment, as discussed further below. In any case, the fluid layer(s) lie atop a flat, rigid floor that covers a square array of 10 × 10 cylindrical neodymium-iron-boron (NdFeB) grade N52 magnets, arranged with their magnetic fields primarily in the vertical ($\hat{\boldsymbol{z}}$) direction. Their polarities alternate in a checkerboard pattern, and they are spaced $L_f = 25.4$ mm on center. The magnets have diameter 12.7 mm and thickness 3 mm, and the magnetic field near their surface is 0.3 T. Rectangular copper electrodes span two opposite sides of the vessel, and we pass current density $\boldsymbol{J} = J\hat{\boldsymbol{x}}$ between them to drive flow via the Lorentz forces that arise when current flows through a magnetic field. (Here $\hat{\boldsymbol{x}}$ is a unit vector in the x direction.)

To visualize the resulting flow, we seed the test fluid with tracer particles that have density 1.022 g/cm^3 and diameters ranging from 90 to 100 μm (Cospheric UVPMS-BG-1.025). Blue LED lamps illuminate the particles, which fluoresce green. An Emergent HS-4000M camera placed about 0.5 m above the test fluid records particle motion. Its lens (25 mm Fujinon CF25HA-1) is covered with blue filters to reduce glare from the lamps, thereby improving measurement accuracy. Its sensor

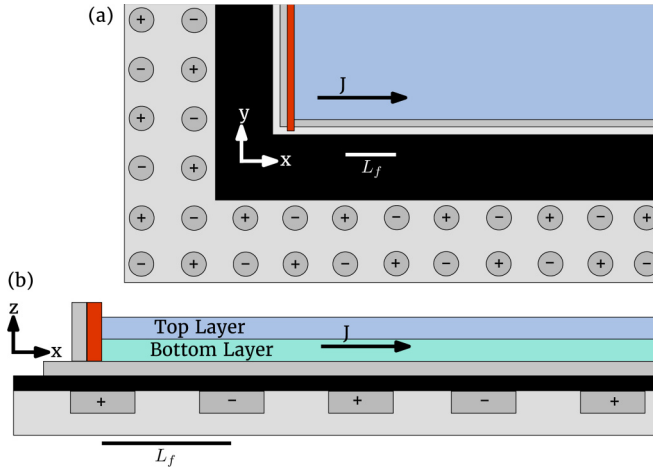

FIG. 1. The experimental apparatus. (a) A view from above shows the magnet grid, glass sheet, and experimental vessel, with one electrode visible at left. Magnet polarity is indicated by + or −. The direction of the current density $\boldsymbol{J}$ is indicated with a black arrow. (b) A cross-section shows two fluid layers, though some experiments described below use only one.

acquires images of size 2048 × 2048 pixels spanning a square field of view with side length between 274 and 319 mm in these experiments, depending on camera placement. These images are cropped such that the entire field of view is within the flow domain, with a buffer of approximately $L_f/2$ removed along the lateral boundaries. We record movies at frame rates ranging from 20 to 120 Hz, sufficient to prevent blurring and allow particle tracking with minimal uncertainty. The duration of each movie is approximately 60 s (i.e., about 1200–7200 frames, depending on frame rate). We use automated particle tracking [42] to measure the positions and velocities of tracer particles within the field of view of the camera; our methods are identical to those described in previous work [30]. We denote the measured velocities $\mathbf{u} = u\hat{\mathbf{x}} + v\hat{\mathbf{y}}$. We test $\mathbf{u}$ for outliers and remove them using a standard universal outlier detection algorithm [43,44]. In the experiments described below, we tracked on the order of 10^4 particles per frame.

We use our apparatus to test the three different experimental configurations described above. In the single-layer configuration, the test fluid is a 6-mm-thick layer of 1 M sulfuric acid with density $\rho_t = 1060\,\mathrm{kg/m^3}$, kinematic viscosity $\nu_t = 1.12 \times 10^{-6}\ \mathrm{m^2/s}$, and electrical conductivity $\sigma = 30\ \mathrm{S/m}$. Accordingly, particles float at the top of the test fluid. We prepare a single-layer experiment by adding tracer particles to a small quantity (∼100 mL) of sulfuric acid and sonicating the particle mixture for a few minutes to break up clumps, then combining the mixture with the remaining sufuric acid in the experimental vessel. We also add a few drops of dish soap as a surfactant, to prevent clumping.

In the immiscible two-layer configuration, the test fluid is again 1 M sulfuric acid. Below the sulfuric acid lies a lubrication layer composed of FC-3283, a fluorinated oil that is an electrical insulator and immiscible with water. Its density is $\rho_b = 1750\,\mathrm{kg/cm^3}$, and its kinematic viscosity is $8.1 \times 10^{-7}\ \mathrm{m^2/s}$. Each of the two layers is 3 mm, for a total thickness of 6 mm. When preparing an immiscible two-layer experiment, we find it most effective to first add an excess amount of each fluid such that the layers are at least 5 mm thick, then remove the excess fluid with a syringe to obtain the desired 3 mm thickness for each layer. A thicker lubricating (bottom) layer helps ensure that when the test (top) layer is poured in, it will not wet the bottom surface of the container, leading to a localized irregularity where the test layer spans the full two-layer depth; gentle pouring also helps prevent this issue. Adding an excess of the test fluid is also necessary to ensure that the layer spans the full breadth of the container; adding sufficient soap to lessen the surface tension helps this issue.

TABLE I. List of experiments reported.

Description	Fluid(s)	$\bar{\nu}$ (m^2/s)	Re range
6-mm single-layer	sulfuric acid	1.12×10^{-6}	$50 \leqslant \mathrm{Re} \leqslant 520$
6-mm miscible	sulfuric acid, water	1.01×10^{-6}	$145 \leqslant \mathrm{Re} \leqslant 520$
6-mm immiscible	FC-3283, sulfuric acid	1.01×10^{-6}	$130 \leqslant \mathrm{Re} \leqslant 740$

In the immiscible configuration, tracer particles float at the top of the test fluid. We do not sonicate the particles first because we find that when pouring in a solution containing particles, there is a tendency for some to get trapped at the interface of the lubricating and test layers. To ensure that all velocity measurements are performed at the free surface of the test fluid, we instead directly add dry particles after the two layers are in place.

On the other hand, in the miscible configuration, tracer particles float at the interface between the test fluid and the freshwater layer above it (the freshwater has density $\rho_t = 1000\,\mathrm{kg/m^3}$ and kinematic viscosity $\nu_t = 9.3 \times 10^{-7}\ \mathrm{m^2/s}$). Comparing out-of-plane motion at the interface (in the miscible configuration) to out-of-plane motion at the free surface (in the single-layer and immiscible configurations) might seem unfair, but we believe it to be the most useful comparison, consistent with the methods of researchers performing thin-layer experiments. In the miscible configuration, we again use the same sulfuric acid solution as in the other two configurations. We prepare a miscible two-layer experiment by adding the freshwater layer first, then sonicating particles in sulfuric acid, combining that mixture with the remaining sulfuric acid, and using a syringe to slowly inject the test fluid with particles below the freshwater layer. We drive syringe injection by gravity, and not the syringe plunger, in an effort to minimize mixing of the two layers. Each of the two layers is 3 mm thick, so the total thickness is 6 mm.

The phenomena we observe in experiments naturally depend on fluid viscosity and, in the miscible and immiscible two-layer configurations, on the viscosity of both layers. To make fair comparisons among the two-layer configurations and the single-layer configuration, we calculate the depth-averaged kinematic viscosity $\bar{\nu}$ of each configuration. In the depth-averaged Navier-Stokes equation that governs the dynamics of thin-layer flow [33,45], $\bar{\nu}$ takes the role played by kinematic viscosity in the usual three-dimensional Navier-Stokes equation. Table I lists the values of $\bar{\nu}$ considered below and provides additional details about each experimental configuration.

Once the configuration is prepared, we typically perform experiments at a range of different Reynolds numbers, varying only the electrical current, maintaining all other parameters, including layer thickness. For all three configurations, the particle densities (particles per unit area), shown in Fig. 2, decrease over time for two reasons: The particles clump together and particles advect to the boundaries where they collect due to the meniscus at the wall. We have countered the particle clumping in the single-layer configuration by stirring vigorously between experiments to break up clumps, effectively increasing the particle density. However, the miscible configuration cannot be stirred since doing so would blur the interface between the test fluid and fresh water. Similarly, we did not stir the immiscible configuration as the top layer is more likely to rupture by doing so. Hence, the particle densities fluctuate in the single-layer configuration, but the densities decrease in both the miscible and immiscible configurations. We attribute the higher particle densities in the miscible configuration to the much lower surface tension experienced by particles. Of course, particle densities also depend on the number of particles added to the test fluid when the configuration is prepared, but the systematic variation with Reynolds number apparent in Fig. 2 suggests that flow processes, not preparation methods, govern long-term particle densities. In all cases, we added an abundance of particles.

Another practical challenge is Joule heating caused by the large electrical currents passing through the test fluid. Raising the temperature of the fluid by 1°C reduces its viscosity and causes a systematic error of about 2% in Re. Joule heating can also drive flow via thermal convection if the temperature

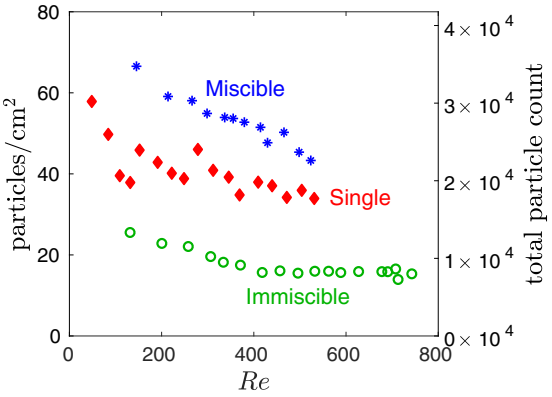

FIG. 2. The particle density (left y axis) and approximate total particle count (right y axis) as a function of Re for the experiments described below.

varies spatially and the temperature differences are great enough. Joule heating is proportional to the square of the current and occurs in all electromagnetically driven thin-layer flows, including some [31] which use much higher currents than what we consider here. Joule heating might be compensated with active cooling of the test fluid, for example, by submerging the flow apparatus in a temperature-controlled water bath [45]. We find that the relatively high electrical conductivity of sulfuric acid significantly reduces Joule heating compared to other commonly used electrolytes, such as copper sulfate [22,33,46], as shown in Fig. 3. Hence, we have intentionally used sulfuric acid for all three configurations in this study to minimize the uncertainty in Re due to temperature variations arising from Joule heating.

Just as the interface between layers in the miscible configuration would be blurred by vigorous stirring between experiments, it is also blurred by diffusion and advection during experiments. Such blurring is visible by eye, so we are careful to perform all miscible experiments before the blurring is significant. For Re $<$ 200, the miscible configuration allows experiments for perhaps 60 min before

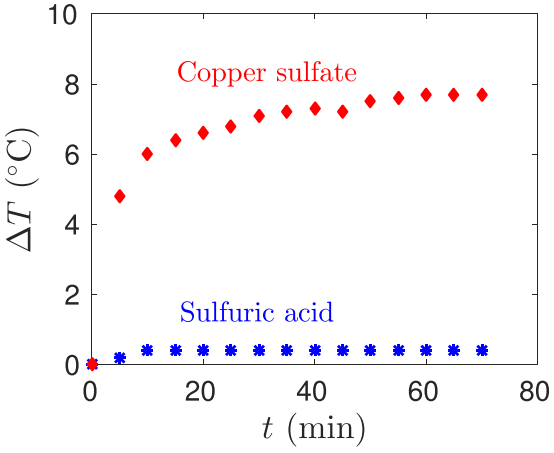

FIG. 3. Variation over time of the horizontal temperature difference ΔT in a single 3-mm layer of fluid, with constant current density $J = 650\ \mathrm{A/m^2}$ applied. We measured the temperature using a thermocouple a few millimeters from the vessel wall. Joule heating is substantially less in sulfuric acid than in copper sulfate because of the higher electrical conductivity. Consequently, experiments using sulfuric acid have less uncertainty in Re.

blurring becomes significant, but at higher values of Re, blurring occurs much more quickly, as discussed below. The single-layer and immiscible configurations have much longer usable lifetimes.

Particle tracking produces a measurement of the position and velocity of each tracked particle in each frame. In order to quantify out-of-plane motion, we project those measurements onto stream function modes, boundary modes, and potential modes, as described in detail previously [30]. Here a brief overview will suffice. Because our experiments involve speeds much less than the speed of sound and layer depths too small for gravity to cause appreciable density variation, we expect the resulting flow to be incompressible. However, to a camera that observes only two components of the full velocity field, out-of-plane motion appears as compressibility: For particles atop the test fluid, downwellings appear to be 2D sinks and upwellings appear to be 2D sources. Thus we can detect out-of-plane motion by quantifying apparent 2D compressibility, i.e., divergence. Mathematically, any vector field with an open boundary can be expressed as the sum of an incompressible (and rotational) part, a compressible (and irrotational) part, and a part that is both incompressible and irrotational. In experiments like ours, the magnitude of the compressible part quantifies out-of-plane motion.

We use least-squares projection to calculate that magnitude. First, we express the compressible part $\boldsymbol{u}^{\text{comp}}$ as the superposition of a set of 2D basis modes that we call the potential modes. Then we express the incompressible part $\boldsymbol{u}^{\text{inc}}$ as the superposition of two sets of 2D basis modes: The stream function modes account for incompressible motions that involve no inflow or outflow at the boundaries, and the boundary modes account for incompressible motions involving inflow and outflow. (The camera's field of view is smaller than the lateral boundaries which contain the test fluid.) As in Ref. [30], the potential modes, stream function modes, and boundary modes are all chosen as eigenfunctions of the Laplacian, but with different boundary conditions for each type of mode. We truncate the (potentially infinite) sets of eigenfunction modes by dropping modes whose characteristic length scale is smaller than some size L_{min}. For all experiments described below, we choose $L_{\text{min}} = L_f/2$. Finally, we use least-squares projection to determine the particular set of mode weights that most accurately represents each velocity field snapshot (each frame). Knowing the modes and the mode weights, we can reconstruct the incompressible part, the compressible part that accounts for out-of-plane motion, or the total flow $\boldsymbol{u}^{\text{total}} = \boldsymbol{u}^{\text{comp}} + \boldsymbol{u}^{\text{inc}}$. Three points deserve emphasis. First, the reconstructed total flow is not identical to the measured flow because modes with characteristic length scales smaller than L_{min} are dropped; essentially, $\boldsymbol{u}^{\text{total}}$ is a smoothed version of the measured flow. Second, like our measurements, both $\boldsymbol{u}^{\text{inc}}$ and $\boldsymbol{u}^{\text{comp}}$ are two-dimensional, having vector components only in the x and y directions. Third, we construct $\boldsymbol{u}^{\text{comp}}$ *without* calculating $\boldsymbol{\nabla} \cdot \boldsymbol{u}$ at all; out-of-plane motion simply projects onto the potential modes but does not project onto the stream function modes or the boundary modes.

Once we have calculated $\boldsymbol{u}^{\text{total}}$, we can quantify the total flow speed of any experiment with the root-mean-square velocity $u^{\text{total}}_{\text{rms}} = \langle (u^{\text{total}})^2 \rangle^{1/2}$, where brackets signify averaging over both space and time. In all cases, the spatial average spans a domain that is $8L_f \times 8L_f$. The temporal average spans at least 8 and as many as 40 characteristic timescales τ, where $\tau = L_f/u^{\text{total}}_{\text{rms}}$. Dimensional arguments predict [46] $u^{\text{total}}_{\text{rms}} \sim J^{1/2}$ in thin-layer experiments. As Fig. 4 shows, that prediction closely matches our observations in all three configurations. To quantify flow speed in dimensionless form, we define the Reynolds number

$$\text{Re} = u^{\text{total}}_{\text{rms}} L_f/\bar{\nu}, \tag{1}$$

again using the depth-averaged viscosity for fair comparison.

III. RESULTS

We measure similar flow fields in all three configurations. In any configuration, when $\text{Re} \lesssim 60$, a steady checkerboard array of vortices is driven by the underlying checkerboard array of magnets. At higher values of Re, the flow deviates from the steady pattern, which becomes unstable. Figure 5 shows the incompressible velocity $\boldsymbol{u}^{\text{inc}}$ and the vorticity $\omega = \boldsymbol{\nabla} \times \boldsymbol{u}^{\text{inc}}$, where $\boldsymbol{\nabla}\times$ is the 2D curl. At $\text{Re} \sim 200$, deviation from the checkerboard is clear, though many of the flow structures still have

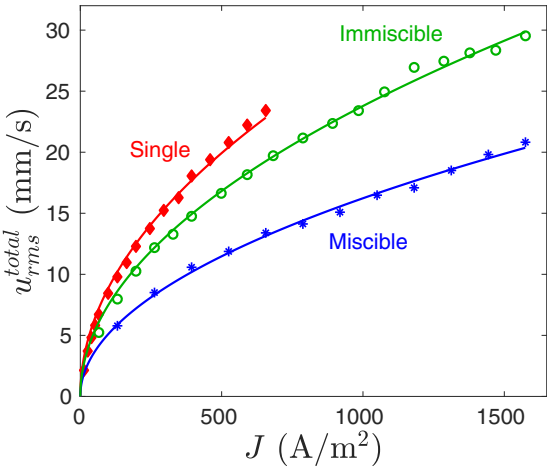

FIG. 4. Root-mean-square velocity $u_{\mathrm{rms}}^{\mathrm{total}}$ varying with current density J for the three different experimental configurations: single-layer, miscible, and immiscible. Uncertainties are the size of the symbols or smaller. The smooth curves, which the measurements match closely, are proportional to $J^{1/2}$.

length scales similar to L_f. At Re $\sim$ 500, the flow deviates more strongly from the steady pattern and exhibits a broader range of length scales.

Using many measurements of flow fields like those shown in Fig. 5 and recorded in different experiments at different Reynolds numbers, we can quantify the total flow in each experiment with the root-mean-square velocity $u_{\mathrm{rms}}^{\mathrm{total}}$, where again we average over both space and time. Likewise we can quantify the magnitude of the incompressible part with its root-mean-square velocity $u_{\mathrm{rms}}^{\mathrm{inc}}$, and we can quantify the magnitude of the compressible part with its root-mean-square velocity $u_{\mathrm{rms}}^{\mathrm{comp}}$. Figure 6 shows the variation of all three quantities with Re, in the single-layer configuration. The total flow magnitude $u_{\mathrm{rms}}^{\mathrm{total}}$ increases linearly with Re by definition, and the incompressible part matches it closely throughout the measured range. The compressible part $u_{\mathrm{rms}}^{\mathrm{comp}}$ increases gradually with Re, with an approximately linear trend throughout the full range of Reynolds numbers that we have tested.

To make a more direct comparison to prior results, we can consider how $u_{\mathrm{rms}}^{\mathrm{total}}$, $u_{\mathrm{rms}}^{\mathrm{inc}}$, and $u_{\mathrm{rms}}^{\mathrm{comp}}$ vary with Re in the miscible configuration, as plotted in Fig. 7. As in the single-layer configuration, $u_{\mathrm{rms}}^{\mathrm{total}}$ and $u_{\mathrm{rms}}^{\mathrm{inc}}$ differ little. The compressible part $u_{\mathrm{rms}}^{\mathrm{comp}}$ shows a critical Reynolds number at $\mathrm{Re}_c = 250$, nearly matching the value $\mathrm{Re}_c = 205$ published previously [30], though the layers are thinner here (each 3 mm instead of each 5 mm). When we extended our experiments to higher values of Re than were explored in the prior work, however, we found that the dynamics changed again in an unexpected way: For Re > 335, $u_{\mathrm{rms}}^{\mathrm{comp}}$ *decreased* as Re increased. Both Ekman pumping and shear instability, the two mechanisms most likely to cause out-of-plane motion, are expected to increase with flow speed. What mechanism could *decrease* out-of-plane motion at high Reynolds numbers?

To address that question, we ran a long, high-Re experiment in the miscible configuration, holding Re $= 440$ for more than 10 min. As shown in Fig. 8, $u_{\mathrm{rms}}^{\mathrm{comp}}$ decreased over time to less than half its initial value, stabilizing after about 6 min. Instantaneous particle distributions, also shown in Fig. 8, agree: Particles are distributed less uniformly near the beginning of the experiment, indicating faster out-of-plane motion, than near the end. The change can be explained by considering the mixing between the freshwater and acid layers. At the beginning of the experiment, particles are gravitationally constrained to move along the interface between a 3-mm acid layer and the 3-mm freshwater layer above it. As vigorous flow blurs the interface and eventually mixes the layers, however, density stratification becomes weak or nonexistent. The particles, which are less dense than the diluted acid, eventually move to the free surface. This effect has been confirmed by directly observing the flow by eye: It is evident in the laboratory that particles occupy a wider range of

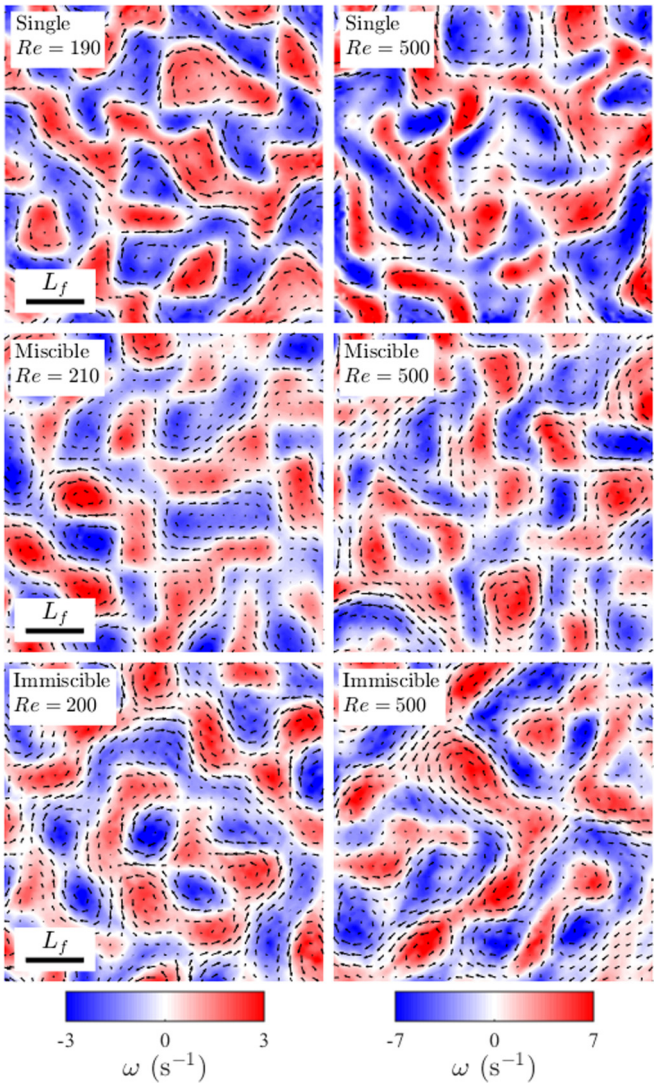

FIG. 5. Instantaneous flow fields during experiments using each of the three different Q2D configurations, recorded at two different values of Re. Arrows indicate $\boldsymbol{u}^{\text{inc}}$, and color indicates vorticity ω. Both fields have been interpolated onto a regular grid, using measurements at individual particles whose locations are irregular. Flow fields at similar values of Re have similar structure in all three configurations.

depths as high-Re experiments progress. Our measurements suggest that at Re = 440, the miscible configuration transitions to the single-layer configuration in about 6 min, and there is a greater out-of-plane motion for the interface of the miscible configuration than at the free surface of the single-layer configuration.

The same mechanism explains the unexpected decrease in $u_{\text{rms}}^{\text{comp}}$ at high Re, shown in Fig. 7. We performed those experiments in order of increasing Re, and by the time of the last six experiments, the two miscible layers had mixed too much for faithful comparison to earlier experiments. We exclude those last five experiments from further analysis.

Researchers using the miscible configuration should be cautious of blurred interfaces. The miscible configuration is viable as long as the time required to blur the interface is much greater than the duration of the experiment. Figure 8 shows the blurring time to be on the order of 2 min for

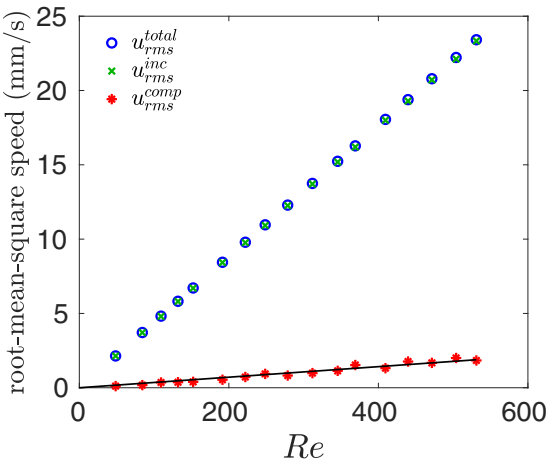

FIG. 6. The three different parts of the velocity, $u_{\mathrm{rms}}^{\mathrm{comp}}$, $u_{\mathrm{rms}}^{\mathrm{inc}}$, and $u_{\mathrm{rms}}^{\mathrm{total}}$, varying with Re for the 6-mm single-layer configuration. The quantity $u_{\mathrm{rms}}^{\mathrm{total}}$ is exactly linear by definition, according to Eq. (1). The compressible part increases gradually with Re, with an approximately linear trend. Uncertainties are the size of the symbols or smaller.

experiments with Re = 440. We expect the blurring time to be shorter at higher Reynolds numbers and longer at lower Reynolds numbers. Figure 7 suggests that the blurring time at Re $<$ 335 is much greater than the 60-s duration typically used for each data point in our experiments. That suggestion is consistent with our empirical experience that the interface becomes visibly blurred after about 60 min of experiments at Re $\leqslant$ 200. Interface blurring does not occur in the single-layer and immiscible configurations.

Sulfuric acid has a slightly higher mass diffusivity than other commonly used electrolytes, such as copper sulfate or sodium chloride [30], which might cause the interface to blur more quickly in configurations with sulfuric acid. On the other hand, the higher electrical conductivity of sulfuric

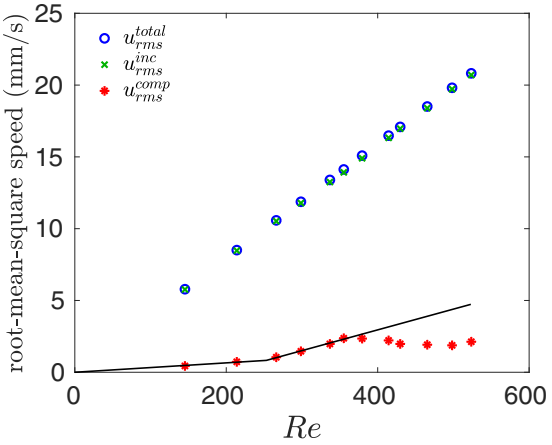

FIG. 7. The three different parts of the velocity, $u_{\mathrm{rms}}^{\mathrm{comp}}$, $u_{\mathrm{rms}}^{\mathrm{inc}}$, and $u_{\mathrm{rms}}^{\mathrm{total}}$, varying with Re for the 6-mm miscible configuration. The quantity $u_{\mathrm{rms}}^{\mathrm{total}}$ is exactly linear by definition, according to Eq. (1). The compressible part strengthens more rapidly when Re $>$ 250, consistent with the onset of an instability. However, the compressible part weakens slightly at larger values of Re, suggesting another mechanism takes effect. Uncertainties are the size of the symbols or smaller.

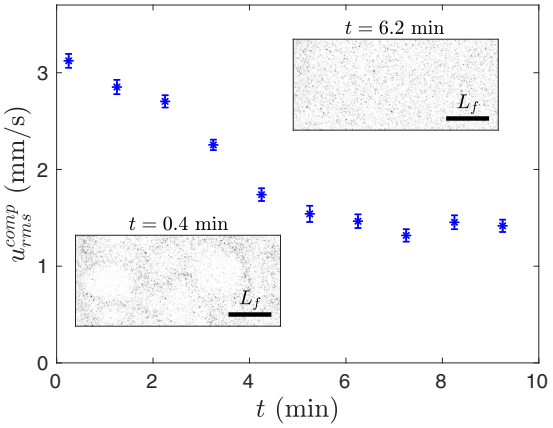

FIG. 8. The compressible part $u_{\mathrm{rms}}^{\mathrm{comp}}$ weakens over time in an experiment using the 6-mm miscible configuration at $\mathrm{Re} = 440$. Insets show instantaneous particle distributions consistent with the weakening of out-of-plane motion: Particle uniformity increases with time. At this high Re, the miscible configuration mixes and effectively becomes a single-layer configuration in about 6 min. Uncertainty bars indicate the standard error of the mean.

acid reduces Joule heating which drives buoyant flow that blurs the interface. Future work might disentangle these two effects to determine which solution is less susceptible to interface blurring. We also note that it is not obvious what difference in densities for the test fluid and freshwater layers is ideal, and it is possible that varying the difference in the densities may change the timescale for interface blurring.

Examining the total flow, incompressible part, and compressible part of experiments using the single-layer and miscible configurations revealed a critical Reynolds number and interface blurring for only the miscible configuration. We now continue to the primary goal of our study, comparing out-of-plane motion in the three different configurations. As shown above, all these experiments approximate two-dimensionality well enough that $u_{\mathrm{rms}}^{\mathrm{total}}$ and $u_{\mathrm{rms}}^{\mathrm{inc}}$ have similar magnitude. Accordingly, we focus next on $u_{\mathrm{rms}}^{\mathrm{comp}}$, which reveals the differences. Figure 9 plots that quantity, over a range of Reynolds numbers, for all three configurations. All measurements fall near the same line for $\mathrm{Re} \leqslant 270$. As Re increases further, the miscible configuration deviates from that line. The single-layer and immiscible configurations, however, do not have any clear critical Reynolds number in the range of Reynolds numbers tested: $u_{\mathrm{rms}}^{\mathrm{comp}}$ increases with a consistent, nearly linear trend. Out-of-plane motion in the miscible configuration has nearly the same magnitude as in the single-layer and immiscible configurations for ranges of Re below $\mathrm{Re}_c = 250$. For ranges of Re above the critical value, the miscible configuration has more out-of-plane motion than the single-layer and immiscible configurations. For $\mathrm{Re} \gtrsim 400$, the single-layer configuration appears to have slightly less out-of-plane motion than the immiscible configuration.

To quantify the out-of-plane motion in dimensionless form, we can normalize its magnitude by the total flow magnitude. Figure 10 shows the variation of $u_{\mathrm{rms}}^{\mathrm{comp}}/u_{\mathrm{rms}}^{\mathrm{total}}$ with Re. The dominant trends are the same as in Fig. 9: All three configurations have out-of-plane motion of similar magnitude until Re grows beyond its critical value and out-of-plane motion grows rapidly for the miscible configuration. Again, the single-layer configuration appears to have somewhat less out-of-plane motion than the immiscible configuration.

Prior studies by Akkermans *et al.* [38,40] quantified out-of-plane motion using the normalized divergence, defined as

$$\Lambda = \frac{h \int\int |\nabla \cdot \mathbf{u}|\, dx\, dy}{L_f \int\int |\nabla \times \mathbf{u}|\, dx\, dy}, \tag{2}$$

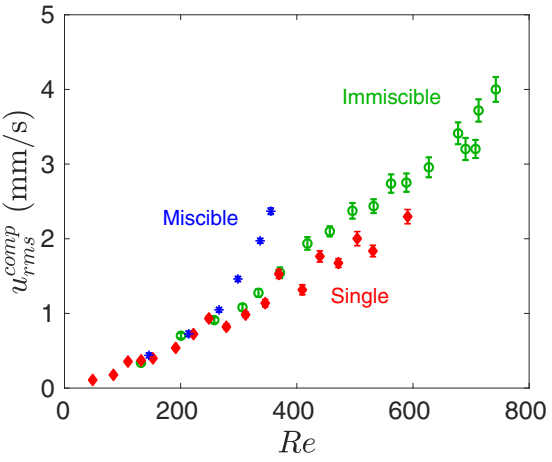

FIG. 9. Variation of the compressible part $u_{\text{rms}}^{\text{comp}}$ with Re for all three configurations. All are similar when Re is low. The miscible configuration displays a critical value of Re, above which out-of-plane motions strengthen rapidly as Re increases. The single-layer and immiscible configurations apparently have no critical value for $\text{Re} < 520$ and $\text{Re} < 740$, respectively. Uncertainty bars indicate the standard error of the mean.

where h is the thickness of the test layer ($h = 3$ mm for the miscible and immiscible configurations and $h = 6$ mm for the single-layer configuration). The normalized divergence provides a measure of out-of-plane motion that is dimensionless like $u_{\text{rms}}^{\text{comp}}/u_{\text{rms}}^{\text{total}}$, but unlike that quantity, requires calculating the divergence directly. Finding agreement between $u_{\text{rms}}^{\text{comp}}/u_{\text{rms}}^{\text{total}}$ and Λ would therefore increase our confidence, particularly if the velocity fields used in each calculation were obtained through different image analysis methods. Hence, we reprocessed our images using particle image velocimetry [47] and calculated Λ using a fourth-order numerical differentiation scheme to accurately evaluate $\boldsymbol{\nabla} \cdot \mathbf{u}$ and $\boldsymbol{\nabla} \times \mathbf{u}$. Figure 11 shows the variation of Λ with Re for all three configurations. Its trends are similar to those of $u_{\text{rms}}^{\text{comp}}/u_{\text{rms}}^{\text{total}}$, shown in Fig. 10: The normalized divergence of the miscible configuration increases sharply above its critical Reynolds number. The normalized divergence of the single-layer and immiscible configurations increases only gradually with Re, showing no obvious

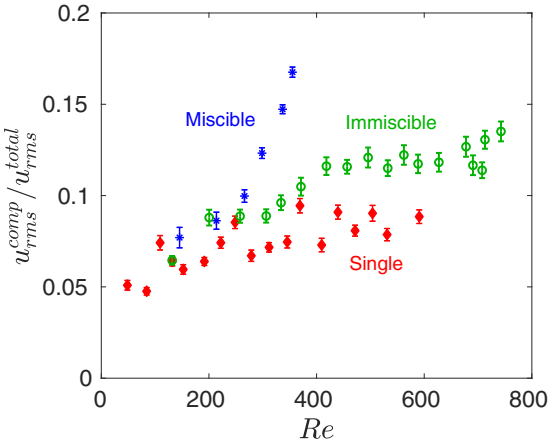

FIG. 10. Variation of the normalized compressible part $u_{\text{rms}}^{\text{comp}}/u_{\text{rms}}^{\text{total}}$ with Re for all three configurations. Trends are consistent with Fig. 9, but normalization makes differences among the three configurations clearer. Uncertainty bars indicate the standard error of the mean.

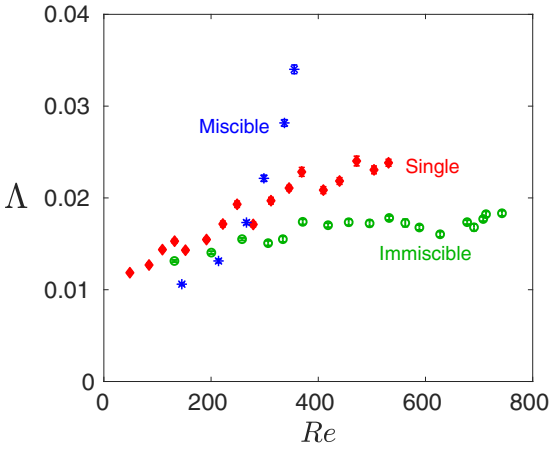

FIG. 11. Variation of the normalized divergence Λ with Re for all three configurations. Trends agree well with Fig. 10. Uncertainty bars indicate the standard error of the mean.

critical Reynolds number. The values of Λ for the immiscible configuration, however, are lower than those of the single-layer configuration, which differs from the trends in Figs. 9 and 10.

The results presented thus far consistently suggest that for $\mathrm{Re} > \mathrm{Re}_c = 250$, the miscible configuration undergoes a transition which leads to a greater rate of increase for the out-of-plane motion. This transition is likely due to a shear instability, as discussed in prior work [46]. We reasoned that this transition may be present in the miscible configuration, but not in the single-layer and immiscible configurations, because of increased shear present in the former case. To test this hypothesis, we computed the normalized velocity profile along the vertical direction $P(z)$ and

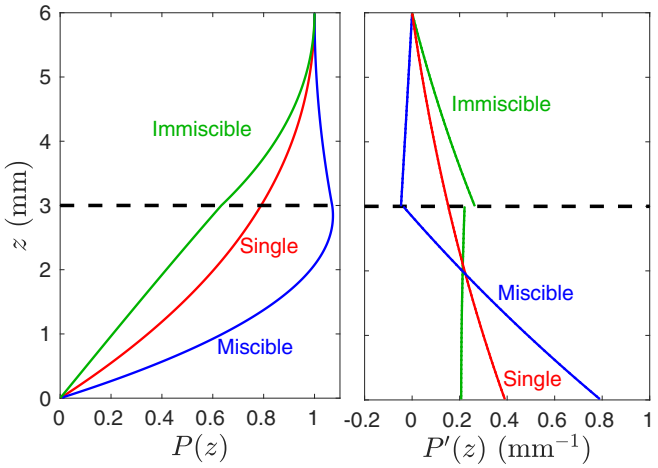

FIG. 12. The normalized vertical velocity profile $P(z)$ (left plot) and the spatial derivative of the normalized vertical velocity profile $P'(z) = \frac{d}{dz}P(z)$ (right plot), both computed using the methods discussed in Suri *et al.* [33]. The horizontal dashed line indicates the boundary of the two layers for the miscible and immiscible configurations. The maximum shear in the miscible configuration is approximately twice that of the single-layer configuration and more than twice that of the immiscible configuration, which may explain the occurrence of a shear instability in only the former case. The discontinuity in $P'(z)$ at $z = 3$ mm for the miscible and immiscible configurations is a consequence of continuity of shear stress at the interface of the two different fluids.

the shear along the vertical direction $P'(z)$ following the methodology of Suri *et al.* [33]. The normalized velocity profiles and shear for the three different configurations are shown in Fig. 12. Note that the discontinuity in $P'(z)$ at $z = 3$ mm for the miscible and immiscible configurations is a consequence of continuity of shear stress at the interface of the two different fluids, which must satisfy $\mu_b P'(h^-) = \mu_t P'(h^+)$, where μ_b and μ_t are the dynamic viscosities of the sulfuric acid and fresh water, respectively. As anticipated, the miscible configuration exhibits the largest shear among the three configurations, reaching values near the bottom surface of the container ($z = 0$ mm) which are approximately two and four times those of the single-layer and immisible configurations, respectively. This large shear is present only in the bottom, driven layer of the miscible configuration, which is positioned between the bottom surface of the container (where there is zero velocity due to the no-slip boundary condition) and the nonforced freshwater above (which is driven due to viscous coupling with the bottom layer). The velocity profiles for the single-layer and immiscible configurations are fairly similar to one another, with substantially less shear than the miscible case.

IV. SUMMARY AND CONCLUSIONS

In summary, we have compared the fidelity of three different experimental configurations intended to model 2D flow. The miscible two-layer configuration exhibited a critical Reynolds number, above which out-of-plane motion increased more rapidly with Re. We found a critical Reynolds number of $\mathrm{Re}_c = 250$ using a 6-mm total fluid depth, which is higher than the value of $\mathrm{Re}_c = 205$ previously found using a 10-mm total fluid depth [46]. This suggests that thinner layers may in fact behave more two-dimensionally and Re_c may correspondingly vary. The single-layer and immiscible configurations exhibited no critical Reynolds number. We quantified out-of-plane motion using two established methods, projection onto stream function modes [30] and normalized divergence [38,40], and we found the same trends with both methods. We showed that vigorous flow can quickly blur the interface between layers in the miscible configuration (within 2 min at $\mathrm{Re} = 440$), causing a transition from a miscible to a single-layer configuration in about 6 min. We believe our discussion is the first substantial treatment of interface blurring as a factor relevant to out-of-plane motion. If the transition to stronger out-of-plane motion that we observe for the miscible configuration is in fact a shear instability, we hypothesize that this is a consequence of the shear along the vertical direction, which our modeling suggests is greater for the miscible configuration than the other two configurations.

In light of our findings, we recommend that experimentalists avoid the miscible configuration for $\mathrm{Re} \gtrsim 200$; for $\mathrm{Re} \lesssim 200$, the miscible configuration may be advantageous as it minimizes out-of-plane motion well, while also reducing clumping of tracer particles which facilitates high particle densities for particle tracking. The results obtained using the projection algorithm (Figs. 9 and 10) and the measured in-plane divergence Λ (Fig. 11) both suggest that the single-layer and immiscible configurations perform similarly well, though we cannot confidently conclude which performs better. This highlights one of the difficulties in quantifying out-of-plane motion using 2D planar measurements: It is difficult to discern true out-of-plane motion from inaccuracies in velocity measurements. Nonetheless, the comparable levels of out-of-plane motion that we measure for the single-layer and immiscible configurations bring into doubt the long-standing assumption that stratification enhances two-dimensionality. Akkermans *et al.* [40] reached a similar conclusion, finding that for a transiently driven dipolar vortex, the immiscible configuration exhibits largely the same three-dimensional vortical structure as the single-layer configuration, and thus does not provide a substantial improvement. Hence, the single-layer configuration may be preferable since it is more convenient to work with. On the other hand, the immiscible configuration allows tuning the vertical shear by adjusting the viscosities of the two layers, as noted previously [33].

The out-of-plane motion driven in Kolmogorov flow, triangular lattices, and quasirandom arrangements might be quantified in future work. The dependence of out-of-plane motion on layer depth might also be considered. Fluorescent Janus particles, half hydrophobic and half hydrophilic, might clump less in the immiscible configuration, if such particles are available. Finally, future

experiments could be performed to obtain measurements at multiple depths (for any of the three configurations) to test the assumptions used to derive the depth-averaged momentum equation and vertical velocity profiles [33,45]. Such a test may be simpler for the miscible and immiscible configurations, as the interface and free surface could be separately seeded and illuminated without requiring a laser sheet.

ACKNOWLEDGMENT

We thank Balachandra Suri for sharing his code for computing the depth-averaged parameters and vertical velocity profiles.

[1] P. B. Rhines, Geostrophic turbulence, Annu. Rev. Fluid Mech. **11**, 401 (1979).
[2] J. Proudman, On the motion of solids in a liquid possessing vorticity, Proc. R. Soc. London, Ser. A **92**, 408 (1916).
[3] H. P. Greenspan, *The Theory of Rotating Fluids*, Cambridge Monographs on Mechanics and Applied Mathematics (Cambridge University Press, London, 1968).
[4] A. Tilgner, Zonal Wind Driven by Inertial Modes, Phys. Rev. Lett. **99**, 194501 (2007).
[5] L. M. Smith, J. R. Chasnov, and F. Waleffe, Crossover from Two- to Three-Dimensional Turbulence, Phys. Rev. Lett. **77**, 2467 (1996).
[6] U. Burr and U. Müller, Rayleigh-Bénard convection in liquid metal layers under the influence of a horizontal magnetic field, J. Fluid Mech. **453**, 345 (2002).
[7] D. H. Kelley and D. R. Sadoway, Mixing in a liquid metal electrode, Phys. Fluids **26**, 057102 (2014).
[8] R. H. Kraichnan, Inertial ranges in two-dimensional turbulence, Phys. Fluids **10**, 1417 (1967).
[9] C. E. Leith, Diffusion approximation for two-dimensional turbulence, Phys. Fluids **11**, 671 (1968).
[10] G. K. Batchelor, Computation of the energy spectrum in homogeneous two-dimensional turbulence, Phys. Fluids **12**, 233 (1969).
[11] G. Haller and G. Yuan, Lagrangian coherent structures and mixing in two-dimensional turbulence, Physica D (Amsterdam, Neth.) **147**, 352 (2000).
[12] D. H. Kelley, M. R. Allshouse, and N. T. Ouellette, Lagrangian coherent structures separate dynamically distinct regions in fluid flows, Phys. Rev. E **88**, 013017 (2013).
[13] N. T. Ouellette, C. A. R. Hogg, and Y. Liao, Correlating Lagrangian structures with forcing in two-dimensional flow, Phys. Fluids **28**, 015105 (2016).
[14] G. J. Chandler and R. R. Kerswell, Invariant recurrent solutions embedded in a turbulent two-dimensional Kolmogorov flow, J. Fluid Mech. **722**, 554 (2013).
[15] D. Lucas and R. R. Kerswell, Recurrent flow analysis in spatiotemporally chaotic two-dimensional Kolmogorov flow, Phys. Fluids **27**, 045106 (2015).
[16] B. Suri, J. Tithof, R. O. Grigoriev, and M. F. Schatz, Forecasting Fluid Flows using the Geometry of Turbulence, Phys. Rev. Lett. **118**, 114501 (2017).
[17] H. Kellay and W. I. Goldburg, Two-dimensional turbulence: A review of some recent experiments, Rep. Prog. Phys. **65**, 845 (2002).
[18] H. Kellay, X. I. Wu, and W. I. Goldburg, Experiments with Turbulent Soap Films, Phys. Rev. Lett. **74**, 3975 (1995).
[19] M. A. Rutgers, Forced 2D Turbulence: Experimental Evidence of Simultaneous Inverse Energy and Forward Enstrophy Cascades, Phys. Rev. Lett. **81**, 2244 (1998).
[20] J. M. Burgess, C. Bizon, W. D. McCormick, J. B. Swift, and H. L. Swinney, Instability of the Kolmogorov flow in a soap film, Phys. Rev. E **60**, 715 (1999).
[21] M. K. Rivera, W. B. Daniel, S. Y. Chen, and R. E. Ecke, Energy and Enstrophy Transfer in Decaying Two-Dimensional Turbulence, Phys. Rev. Lett. **90**, 104502 (2003).
[22] N. F. Bondarenko, M. Z. Gak, and F. V. Dolzhanskiy, Laboratory and theoretical models of plane periodic flows, Izv. Akad. Nauk SSSR, Fiz. Atmos. Okeana **15**, 711 (1979).

[23] P. Tabeling, S. Burkhart, O. Cardoso, and H. Willaime, Experimental Study of Freely Decaying Two-Dimensional Turbulence, Phys. Rev. Lett. **67**, 3772 (1991).
[24] P. Vorobieff and R. E. Ecke, Fluid instabilities and wakes in a soap-film tunnel, Am. J. Phys. **67**, 394 (1999).
[25] T. H. Solomon and I. Mezic, Uniform resonant chaotic mixing in fluid flows, Nature (London) **425**, 376 (2003).
[26] N. T. Ouellette and J. P. Gollub, Curvature Fields, Topology, and the Dynamics of Spatiotemporal Chaos, Phys. Rev. Lett. **99**, 194502 (2007).
[27] D. Marteau, O. Cardoso, and P. Tabeling, Equilibrium states of two-dimensional turbulence: An experimental study, Phys. Rev. E **51**, 5124 (1995).
[28] D. Rothstein, E. Henry, and J. P. Gollub, Persistent patterns in transient chaotic fluid mixing, Nature (London) **401**, 770 (1999).
[29] G. A. Voth, G. Haller, and J. P. Gollub, Experimental Measurements of Stretching Fields in Fluid Mixing, Phys. Rev. Lett. **88**, 254501 (2002).
[30] D. H. Kelley and N. T. Ouellette, Onset of three-dimensionality in electromagnetic thin-layer flows, Phys. Fluids **23**, 045103 (2011).
[31] M. K. Rivera and R. E. Ecke, Pair Dispersion and Doubling Time Statistics in Two-Dimensional Turbulence, Phys. Rev. Lett. **95**, 194503 (2005).
[32] M. J. Twardos, P. E. Arratia, M. K. Rivera, G. A. Voth, J. P. Gollub, and R. E. Ecke, Stretching fields and mixing near the transition to nonperiodic two-dimensional flow, Phys. Rev. E **77**, 056315 (2008).
[33] B. Suri, J. Tithof, R. Mitchell Jr., R. O. Grigoriev, and M. F. Schatz, Velocity profile in a two-layer Kolmogorov-like flow, Phys. Fluids **26**, 053601 (2014).
[34] H. J. H. Clercx and G. J. F. van Heijst, Two-dimensional Navier-Stokes turbulence in bounded domains, Appl. Mech. Rev. **62**, 020802 (2009).
[35] J. Paret, D. Marteau, O. Paireau, and P. Tabeling, Are flows electromagnetically forced in thin stratified layers two dimensional? Phys. Fluids **9**, 3102 (1997).
[36] B. Jüttner, D. Marteau, P. Tabeling, and A. Thess, Numerical simulations of experiments on quasi-two-dimensional turbulence, Phys. Rev. E **55**, 5479 (1997).
[37] M. P. Satijn, A. W. Cense, R. Verzicco, H. J. H. Clercx, and G. J. F. van Heijst, Three-dimensional structure and decay properties of vortices in shallow fluid layers, Phys. Fluids **13**, 1932 (2001).
[38] R. A. D. Akkermans, A. R. Cieslik, L. P. J. Kamp, R. R. Trieling, H. J. H. Clercx, and G. J. F. van Heijst, The three-dimensional structure of an electromagnetically generated dipolar vortex in a shallow fluid layer, Phys. Fluids **20**, 116601 (2008).
[39] R. A. D. Akkermans, L. P. J. Kamp, H. J. H. Clercx, and G. J. F. van Heijst, Intrinsic three-dimensionality in electromagnetically driven shallow flows, Europhys. Lett. **83**, 24001 (2008).
[40] R. A. D. Akkermans, L. P. J. Kamp, H. J. H. Clercx, and G. J. F. van Heijst, Three-dimensional flow in electromagnetically driven shallow two-layer fluids, Phys. Rev. E **82**, 026314 (2010).
[41] F. Lekien, C. Coulliette, R. Bank, and J. Marsden, Open-boundary modal analysis: Interpolation, extrapolation, and filtering, J. Geophys. Res. **109**, C12004 (2004).
[42] N. T. Ouellette, H. Xu, and E. Bodenschatz, A quantitative study of three-dimensional Lagrangian particle tracking algorithms, Exp. Fluids **40**, 301 (2006).
[43] J. Westerweel and F. Scarano, Universal outlier detection for PIV data, Exp. Fluids **39**, 1096 (2005).
[44] J. Duncan, D. Dabiri, J. Hove, and M. Gharib, Universal outlier detection for particle image velocimetry (PIV) and particle tracking velocimetry (PTV) data, Meas. Sci. Technol. **21**, 057002 (2010).
[45] J. Tithof, B. Suri, R. K. Pallantla, R. O. Grigoriev, and M. F. Schatz, Bifurcations in a quasi-two-dimensional Kolmogorov-like flow, J. Fluid Mech. **828**, 837 (2017).
[46] D. H. Kelley and N. T. Ouellette, Using particle tracking to measure flow instabilities in an undergraduate laboratory experiment, Am. J. Phys. **79**, 267 (2011).
[47] D. Brady, J. Charonko, and P. P. Vlachos, QI—quantitative imaging (PIV and more) https://sourceforge.net/projects/qi-tools/.